

A theoretical study of collective plasmonic excitations in double-layer silicene at finite temperature ^{EP}

Cite as: J. Appl. Phys. **125**, 104302 (2019); <https://doi.org/10.1063/1.5083200>

Submitted: 29 November 2018 . Accepted: 28 February 2019 . Published Online: 14 March 2019

N. Dadkhah, ^{id} T. Vazifehshenas, M. Farmanbar, and T. Salavati-fard

COLLECTIONS

^{EP} This paper was selected as an Editor's Pick



View Online



Export Citation



CrossMark

ARTICLES YOU MAY BE INTERESTED IN

[On the quasistatic optimal plasmonic resonances in lossy media](#)

Journal of Applied Physics **125**, 103105 (2019); <https://doi.org/10.1063/1.5085721>

[Effects of surface recombination on the charge collection in h-BN neutron detectors](#)

Journal of Applied Physics **125**, 104501 (2019); <https://doi.org/10.1063/1.5089138>

[Silicon surface passivation by transparent conductive zinc oxide](#)

Journal of Applied Physics **125**, 105305 (2019); <https://doi.org/10.1063/1.5054166>

Webinar
How to Characterize Magnetic Materials Using Lock-in Amplifiers

Zurich Instruments

CRYOGENIC

Register now

A theoretical study of collective plasmonic excitations in double-layer silicene at finite temperature

Cite as: J. Appl. Phys. **125**, 104302 (2019); doi: [10.1063/1.5083200](https://doi.org/10.1063/1.5083200)

Submitted: 29 November 2018 · Accepted: 28 February 2019 ·

Published Online: 14 March 2019



N. Dadkhah,¹ T. Vazifeshenas,^{1,a)}  M. Farmanbar,² and T. Salavati-fard^{3,4}

AFFILIATIONS

¹Department of Physics, Shahid Beheshti University, G. C., Evin, Tehran 1983969411, Iran

²Faculty of Science and Technology and MESA+ Institute for Nanotechnology, University of Twente, P.O. Box 217, 7500 AE Enschede, The Netherlands

³Department of Physics and Astronomy, University of Delaware, Newark, Delaware 19716, USA

⁴Department of Chemical and Biomolecular Engineering, University of Houston, Houston, Texas 77204, USA

^{a)}Electronic mail: t-vazifeh@sbu.ac.ir

ABSTRACT

We explore the temperature-dependent plasmonic modes of an n-doped double-layer silicene system which is composed of two spatially separated single layers of silicene with a distance large enough to prevent interlayer electron tunneling. By applying an externally applied electric field, we numerically obtain the poles of the loss function within the so-called random phase approximation to investigate the effects of temperature and geometry on the plasmon branches in three different regimes: topological insulator, valley-spin polarized metal, and band insulator. Also, we present the finite-temperature numerical results along with the zero-temperature analytical ones to support a discussion of the distinct effects of the external electric field and temperature on plasmon dispersion. Our results show that at zero temperature both the acoustic and optical modes decrease when the applied electric field is increased and experience a discontinuity at the valley-spin polarized metal phase as the system transitions from a topological insulator to a band insulator. At finite temperature, the optical plasmons are damped around this discontinuity, and the acoustic modes may exhibit a continuous transition. Moreover, while the optical branch of plasmons changes non-monotonically and noticeably with temperature, the acoustic branch dispersion displays a negligible growth with temperature for all phases of silicene. Furthermore, our finite-temperature results indicate that the dependency of two plasmonic branches on the interlayer separation is not affected by temperature at long wavelengths; the acoustic mode energy varies slightly with an increase in the interlayer distance, whereas the optical mode remains unchanged.

Published under license by AIP Publishing. <https://doi.org/10.1063/1.5083200>

I. INTRODUCTION

The advent of two-dimensional (2D) materials has sparked a considerable scientific interest due to their unique properties and their potential for applications in electronic, spintronic, valleytronic, optoelectronic, and plasmonic devices. Silicene, the silicon counterpart of graphene, has received much attention in recent years both theoretically¹⁻⁷ and experimentally.⁸⁻¹⁷ Like graphene, silicene is an atomically-thin sheet of silicon atoms arranged in a honeycomb structure; however, unlike graphene, silicene does not hold a planar structure. A small out-of-plane buckling of the silicene structure due to the sp^3 hybridization results in a system of

two sublattices (A and B) which lie in two parallel planes separated by a vertical distance $2l = 0.46 \text{ \AA}$.^{2,18,19} The novel properties of graphene arise from its band structure, in which the valence and conduction bands meet at Dirac points (K and K') in the first Brillouin zone with a well-defined linear energy dispersion relation around these points: $E(\mathbf{k}) = \pm \hbar v_F |\mathbf{k}|$ with $v_F = 10^6 \text{ m/s}$ and $\hbar \mathbf{k}$ being the carrier momentum. The strong spin-orbit interaction in silicene along with the buckled structure induces a nonzero bandgap, $2\Delta_{SO}$, of about a few meV. The buckled structure of silicene provides a new possibility of establishing a potential difference between sublattices A and B, by applying an external out-of-plane electric

field E_z . Interestingly, this feature allows for tuning the bandgap of silicene and distinguishing between the different phases, namely, topological insulator (TI), valley-spin polarized metal (VSPM), and band insulator (BI). Clearly, this offers a benefit over graphene.

Furthermore, for the biased silicene-like materials, some valley-dependent properties can be expected in the presence of an exchange field. Silicene's extra spin and valley degrees of freedom makes it a very versatile material. Silicene can be effectively used as a source of nearly 100% spin-polarized electrons²⁰ and as a valley-selective spin filter.^{21–23} Moreover, silicene can probably be integrated into the current silicon-based electronics, which makes it a promising material for future electronic applications.²⁴

Considerable progress in fabrication techniques has made the synthesis of double-layer 2D structures more tenable. A double-layer structure is composed of two parallel electron or hole gas systems which are kept in close vicinity and are coupled through the Coulomb interaction. This class of 2D structures demands special attention due to exciting many-body phenomena that they can display, such as the coupled collective excitations, Coulomb drag, fractional quantized Hall effect,^{25–27} and more. The interlayer interaction accounts for unique effects in correlated double-layer systems, which have been extensively investigated in double-layer GaAs-based quantum wells, double-layer graphene, and double-layer phosphorene structures.^{28–36}

Plasmons, the collective excitations of an interacting electron or hole gas system, can be pictured as different modes of charge density oscillations. Plasmon branches are the central concept of the rapidly developing field of plasmonics which deals with light-matter (photon-surface plasmon) interactions and their technologically significant consequences. The plasmonic dispersion relations, which reveal the wave vector-dependent modes, can be theoretically obtained from zeros of the dynamical dielectric function of the system^{37,38} and may be observed by inelastic light scattering spectroscopy, frequency domain far-infrared spectroscopy, or inelastic electron scattering spectroscopy.³² The well-behaved plasmon modes lie outside the single-particle excitation (SPE) region. However, those modes entering this region experience the Landau damping.

The plasma oscillations of single-layer silicene (SLS) have already been calculated at both zero temperature and finite temperature with and without a perpendicularly applied electric field.^{39–42} It has been shown that, in an extrinsic SLS, the plasma oscillations follow a \sqrt{q} behavior in the long-wavelength limit at zero temperature for all values of electric field (i.e., all different phases). In addition, the location of the long-wavelength plasmon branch as a function of the applied electric field depends on the position of the Fermi energy with respect to the spin-split bands.^{40,43} These results resemble those of single-layer graphene (SLG) and single-layer gapped graphene (SLGG) with $\Delta_{SO} = 0$ and $\Delta_{SO} \neq 0$, respectively. Moreover, the presence of a small gap in SLGG and various combinations of two gaps in SLS leads to the splitting of the plasmon branch and the appearance of new undamped plasmon modes.^{44,41} On the other hand, in the case of SLG, plasmons decay into particle-hole pairs in the interband portion of the SPE region, while for SLS, both intra- and interband dampings can occur by tuning the external electric field.⁴⁰ The extrinsic (doped) finite-temperature plasmons of SLS have also been studied: as temperature

increases from $T = 0$, the plasmon energy first lowers, reaching a minimum value and then bounces back in both cases of SLS and SLGG.^{42,45}

Similar calculations were performed at zero temperature when both electric and magnetic (exchange) fields were applied.⁴⁶ It is worth pointing out that an exchange field can be induced by positioning ferromagnetic adatoms⁴⁷ on the surface or by employing a ferromagnetic substrate.^{48,49} In the presence of these fields, the SPE region is given a spin-valley texture, which results in the spin-polarized plasmons with zero E_z but finite exchange field and valley-spin-polarized plasmons when both fields are finite. However, it was mentioned that the magnetic field strongly affected the plasmon branch intensity such that it was unlikely to be experimentally observable. Also, the typical \sqrt{q} behavior of long-wavelength plasmons in 2D systems was preserved when the magnetic field was turned on. For shorter wavelengths, although the plasmon dispersion looked different in the presence of a strong magnetic field, it was still possible to tune plasmons to display an approximate \sqrt{q} behavior.⁴⁶ In a recent work, the plasmon-phonon coupling in a valley-spin polarized SLS was investigated and the dispersion relations of hybrid modes were discussed.⁵⁰

Plasma oscillations have also been studied in a doped double-layer graphene at both zero^{32,51–55} and finite^{38,56,57} temperatures within the so-called random phase approximation (RPA). At zero temperature and in the limit of small wave vectors, the plasmon dispersion of the in-phase (optical) branch obeys the $\sim \sqrt{q}$ relation and is independent of the interlayer separation, d . On the other hand, the out-of-phase (acoustic) branch has an $\sim q$ dispersion and depends upon layer distance as $\sim \sqrt{d}$. This long-wavelength behavior of plasmons is identical to that of the conventional double-layer 2D electron gas despite having different dependence on the electron density. Moreover, the plasmonic dispersion for larger wave vectors calculated within the RPA for both systems differs from one another.^{32,54,55} At finite temperature, the frequency of the acoustic mode decreases to $T \approx 0.4T_F$ and then increases afterwards. However, the slope of the growth/decline highly depends on the value of the wave vector. The variation of optical mode energy with temperature is not uniform; it is fair to say that at low wave vectors, the optical branch mimics the behavior of the acoustic branch while at large wave vectors, the frequency of this branch generally increases with increasing temperature.^{38,56}

In this paper, we consider an n-doped double-layer silicene (DLS) system in which two parallel single layers of silicene are placed in a dielectric environment at a distance d from one another, which is short enough to make an effective interaction between them but far enough to guarantee that there will be no electron tunneling. A schematic model of this system is shown in Fig. 1. We investigate the effect of temperature on both plasmon branches with and without the presence of a perpendicular electric field within different regimes. We also study the dependence of the plasmon frequencies on the interlayer distance.

The rest of this paper is organized as follows: In Sec. II, we describe the model and theoretical formalism. In Sec. III, we present the results of calculations and discuss them in detail. Finally, a conclusion is given in Sec. IV.

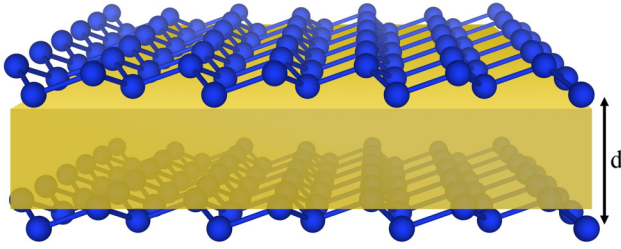


FIG. 1. Schematic view of a double-layer silicene with an interlayer distance of d .

II. THEORY

A. Low-energy Hamiltonian

Focusing on low-energy phenomena, the effective Hamiltonian of a buckled honeycomb structure with an effective intrinsic spin-orbit coupling (SOC) strength Δ_{SO} ($\Delta_{SO} = 3.9$ meV throughout this paper), in the presence of a perpendicular electric field, around the Dirac point K_ξ , is given by^{58–60}

$$\hat{H}_\xi = \hbar v_F (\xi k_x \hat{\tau}_x + k_y \hat{\tau}_y) - \xi \Delta_{SO} \hat{\sigma}_z \hat{\tau}_z + \Delta_z \hat{\tau}_z, \quad (1)$$

where ξ distinguishes the two inequivalent valleys with $\xi = +1$ (-1), representing K (K') point. $\mathbf{k} = (k_x, k_y)$ is the 2D wave vector measured relative to the Dirac points. τ_i and σ_i are Pauli matrices corresponding to (sublattice) pseudospin (written in A-B basis) and the real spin of the system, respectively. They are given as

$$\tau_x = \begin{pmatrix} 0 & 1 \\ 1 & 0 \end{pmatrix}, \tau_y = \begin{pmatrix} 0 & -i \\ i & 0 \end{pmatrix}, \tau_z = \sigma_z = \begin{pmatrix} 1 & 0 \\ 0 & -1 \end{pmatrix}. \quad (2)$$

Further, v_F is the Fermi velocity of the electrons, reported to be 5×10^5 m/s for silicene.^{61,62} Finally, $2\Delta_z$ shows the on-site potential difference between the two sublattices. This low-energy model works quite well for energies between -800 and $+800$ meV.⁶¹

The effects of intrinsic Rashba SOC and electric field induced Rashba SOC are not considerable⁴⁶ and, therefore, are neglected in the Hamiltonian (1). Consequently, spin states are decoupled and the eigenvalues obtained from Eq. (1) are labeled by valley (ξ) and spin (σ) indexes

$$E_{\sigma\xi}(\mathbf{k}) = \lambda \sqrt{\hbar^2 v_F^2 |\mathbf{k}|^2 + \Delta_{\sigma\xi}^2}, \quad (3)$$

where $\Delta_{\sigma\xi} = |\sigma\xi\Delta_{SO} - \Delta_z|$ and $\lambda = \pm 1$ indexes over the conduction (particle) and valence (hole) bands, respectively. It is also helpful to introduce $\Delta_{min} \equiv \Delta_{+,+} = \Delta_{-,-}$ and $\Delta_{max} \equiv \Delta_{+,-} = \Delta_{-,+}$. As can be seen from the above equation, in the absence of an external electric field, there exists a bandgap of $2\Delta_{SO}$. When E_z is turned on and $\Delta_z/\Delta_{SO} < 1$ (TI regime), the bands become spin-split, representing two energy gaps determined by $2\Delta_{min}$ and $2\Delta_{max}$. At $\Delta_z/\Delta_{SO} = 1$

(VSPM regime), the lower bandgap closes; however, by further increase of E_z , it opens up again (BI regime).

B. Collective excitations

For a double-layer system, the location of the undamped plasmon collective modes, in the (ω, q) space, is determined by the zeros of the dielectric tensor, generalized from the single-layer dynamical dielectric function.³⁷ For systems with high electron density, it is reasonable to employ the RPA to calculate the dielectric tensor.³⁸ In this approach, the aforementioned tensor is given by^{37,32}

$$\epsilon_{ij}(\omega, \mathbf{q}) = \delta_{ij} - v_{ij}(\mathbf{q}) \Pi_j^0(\omega, \mathbf{q}), \quad (4)$$

where i and j specify the two layers, $v_{ij}(\mathbf{q})$ is the Fourier component of the bare 2D Coulomb interaction between electrons in layers i and j , and Π_j^0 is the non-interacting dynamical polarization function associated with j th layer. For a double-layer system consisting of two identical layers separated by a distance d , we have $v_{11}(q) = v_{22}(q) = v(q) = 2\pi\alpha/q$ (intralayer interaction) and $v_{12}(q) = v_{21}(q) = v(q)e^{-qd}$ (interlayer interaction)³⁷ in which α is the effective fine structure constant, expressed as $e^2/4\pi\epsilon_0\kappa$ with κ being the effective background dielectric constant. The dimensionless fine structure constant is a measure of the quasiparticle interaction strength.⁶³ The value of fine structure constant has been explored both theoretically⁶³ and experimentally^{64–66} for graphene. There are no such studies for the buckled silicene with the spin-orbit coupling. Here, we use $\kappa = 4$ (assuming a SiO_2 background) to elucidate some interesting features. Finally, $\Pi_i^0 = \Pi_j^0 = \Pi^0$ is given by⁴⁴

$$\begin{aligned} \Pi^0(\omega, q) = & \frac{1}{8\pi^2} \sum_{\sigma, \xi = \pm 1} \int d^2\mathbf{k} \\ & \sum_{\lambda, \lambda' = \pm 1} \left(1 + \lambda\lambda' \frac{\hbar^2 v_F^2 \mathbf{k} \cdot (\mathbf{q} + \mathbf{k}) + \Delta_{\sigma\xi}^2}{E_{\sigma\xi}(\mathbf{k}) E_{\sigma\xi}(\mathbf{k} + \mathbf{q})} \right) \\ & \times \frac{n_F[\lambda E_{\sigma\xi}(\mathbf{k})] - n_F[\lambda' E_{\sigma\xi}(\mathbf{k} + \mathbf{q})]}{\lambda E_{\sigma\xi}(\mathbf{k}) - \lambda' E_{\sigma\xi}(\mathbf{k} + \mathbf{q}) - \omega - i0^+}. \end{aligned} \quad (5)$$

Here, $n_F(E) = 1/[e^{(E-\mu)/k_B T} + 1]$ is the Fermi-Dirac distribution function with μ being the chemical potential which equals to the Fermi energy E_F at $T = 0$. It is important to notice that the upper limit of integration over k is restricted by the low-energy condition. Hence, in the case of identical layers, the plasmon modes can be obtained from the zeros of the following relation:

$$\epsilon(\omega, q) = [1 - v(q)\Pi^0(\omega, q)]^2 - v^2(q)e^{-2qd}\Pi^0(\omega, q). \quad (6)$$

The dynamical dielectric function is generally a complex function of (ω, q) such that ω explicitly has a positive imaginary part, which guarantees that the dynamical physical functions are retarded. For undamped plasmon excitations in the (ω, q) space, both the real $[\Re\epsilon(\omega, q)]$ and imaginary $[\Im\epsilon(\omega, q)]$ parts of the

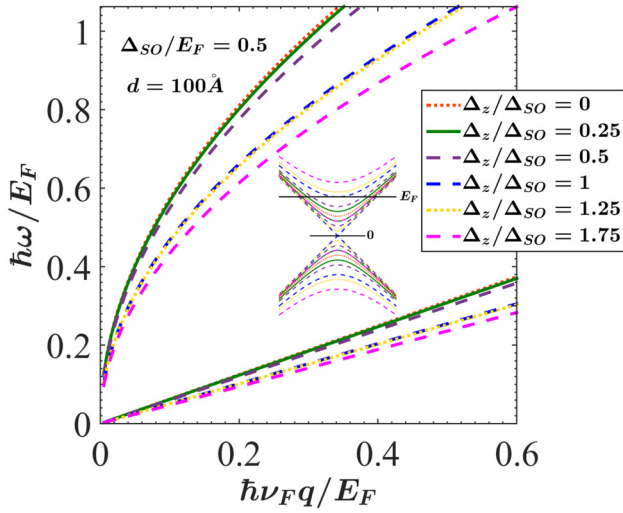


FIG. 2. Zero-temperature plasmon dispersion of a DLS with $d = 100 \text{ \AA}$ for $\Delta_{SO}/E_F = 0.5$ and varying Δ_z at low energies. The inset shows the position of band structure relative to E_F as Δ_z varies.

dielectric function are equal to zero. However, there can be points where $\Re\epsilon(\omega, q) = 0$ but $\Im\epsilon(\omega, q) \neq 0$, which indicates the existence of collective modes at these points but with a finite lifetime due to the nonzero value of $\Im\epsilon$. These types of plasmons decay into particle-hole excitation states. For those points of the (ω, q) plane where $\Im\epsilon(\omega, q) \neq 0$, the single-particle excitations are possible, i.e., a photon with a wave vector q and frequency ω can excite a particle-hole pair in the system. These regions in the (ω, q) space are called SPE spectrum; any collective mode present in SPE will eventually decay (known as the Landau damping). SPE spectrum can be studied as two separate regions corresponding to the inter- and intra-band pair-creation excitations.

At $T = 0$ and in the limit of low energies and momenta, $\hbar\nu_F q \ll \hbar\omega \ll E_F$, the non-interacting polarization function of Eq. (5) has the following analytical form:^{43,44,46}

$$\Pi^0(\omega, q) \approx \sum_{\xi, \sigma = \pm 1} \frac{q^2 E_F}{4\pi\hbar^2 \omega^2} (1 - \Delta_{\xi\sigma}^2/E_F^2) \Theta(E_F - \Delta_{\xi\sigma}). \quad (7)$$

For $qd \ll 1$, Eqs. (6) and (7) give the corresponding plasmon frequencies as

$$\tilde{\omega}_p^{OP} \approx \sqrt{\tilde{\alpha}\tilde{q} \sum_{\sigma, \xi = \pm 1} (1 - \tilde{\Delta}_{\xi\sigma}^2) \Theta(1 - \tilde{\Delta}_{\xi\sigma})}, \quad (8)$$

$$\tilde{\omega}_p^{AP} \approx \tilde{q} \sqrt{\frac{1}{2}\tilde{\alpha}\tilde{d} \sum_{\sigma, \xi = \pm 1} (1 - \tilde{\Delta}_{\xi\sigma}^2) \Theta(1 - \tilde{\Delta}_{\xi\sigma})}, \quad (9)$$

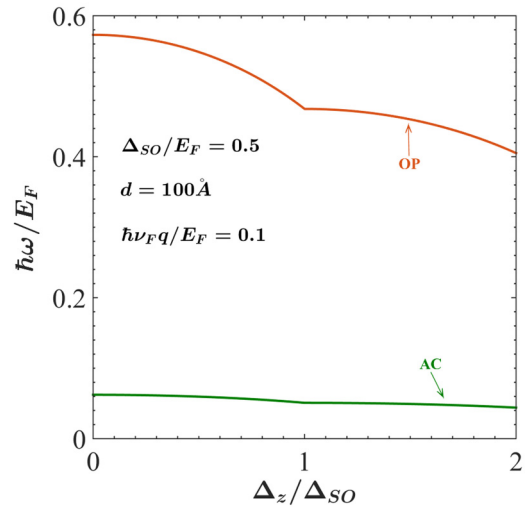


FIG. 3. Zero-temperature plasmon frequency of a DLS as a function of Δ_z with $d = 100 \text{ \AA}$ for $\Delta_{SO}/E_F = 0.5$ and $\tilde{q} = 0.1$ at low energies.

where $\tilde{\alpha} = \alpha/\hbar\nu_F$, $\tilde{d} = (E_F/\hbar\nu_F)d$, $\tilde{\omega} = \hbar\omega/E_F$, $\tilde{q} = \hbar\nu_F q/E_F$, and $\tilde{\Delta}_{\xi\sigma} = \Delta_{\xi\sigma}/E_F$ are all dimensionless parameters.

Equations (8) and (9) reproduce the well-known behavior of plasmons in a double-layer system³² which is shown in Fig. 2 for $\Delta_{SO}/E_F = 0.5$, $d = 100 \text{ \AA}$ and varying Δ_z . The linear (non-linear) branch corresponds to the acoustic (optical) plasmon modes. Here, the Fermi energy sits above both gaps in the TI regime ($\Delta_z/\Delta_{SO} < 1$) and only above the lower gap in the BI regime ($\Delta_z/\Delta_{SO} > 1$). For the latter, Eqs. (8) and (9) show that the plasmon dispersion depends only on the lower bandgap and the upper bandgap plays no role. For this given configuration, the frequencies of both branches decrease as the potential difference increases. However, Fig. 3 shows a discontinuity in the dispersion relations of both branches (which is more pronounced for the optical branch) as the system transitions from TI to BI through the VSPM phase ($\Delta_z/\Delta_{SO} = 1$).

III. RESULTS AND DISCUSSION

The spectral weight associated with a particular plasmon mode is directly proportional to $\Im[\epsilon^{-1}(\omega, q)]$ and is known as the loss function. This quantity, which can be measured experimentally (e.g., in inelastic electron scattering experiments), gives a measure of the absorption of radiation and is an indication of the plasmon creation in the system. Thus, the loss function in the (ω, q) space provides us with branches (poles of the loss function), which identifies both damped and undamped plasmons. In fact, the long-lived plasmons (those that are outside the SPE regions) are δ -function peaks of the loss function, while the damped plasmons (those are inside SPE regions) correspond to the broadened peaks of the loss function.³²

In this section, we first study the effect of temperature and bandgap variations on the SPE regions. In this respect, we need to

numerically calculate Eq. (5). Note that for $T > 0$, the effect of temperature on the chemical potential, μ , must be taken into account. This can be done by assuming that the number of carriers of the system is fixed and μ changes accordingly. Figure 4 demonstrates the dependence of μ/E_F on T/T_F calculated by using numerical methods for $\Delta_{SO}/E_F = 0.5$ and different values of Δ_z/Δ_{SO} .

To investigate the SPE regions in silicene, we plot the imaginary part of the dynamical polarization function for $\Delta_{SO}/E_F = 0.5$ at $T = 0.5T_F$ and $T = T_F$, respectively (see Figs. 5 and 6). The layers are apart by $d = 100 \text{ \AA}$ (this value is used for the rest of calculations, as well) and the applied electric field varies $\Delta_z/\Delta_{SO} = 0, 0.25, 1$, and 1.75 .

The SPE^{Inter} and SPE^{Intra} regions are above and below the $\tilde{\omega} = \tilde{q}$ line, respectively. The SPE boundaries are determined analytically at $T = 0$,⁴⁰ whereas at finite temperature, they can be expressed approximately as

$$\begin{aligned} \tilde{\omega}_{min(max)}^{th(Inter)} &\approx 2\sqrt{(\tilde{q}/2)^2 + (\tilde{\Delta}_{min(max)})^2}, \\ \tilde{\omega}_{min}^{Intra} &\approx 0, \\ \tilde{\omega}_{max}^{Intra} &\approx \tilde{q}. \end{aligned} \quad (10)$$

At a given \tilde{q} , $\tilde{\omega}^{th(Inter)}$ determines the threshold energy for the onset of an interband pair excitation, while $\tilde{\omega}_{max}^{Intra}$ ($\tilde{\omega}_{min}^{Intra}$) gives us the maximum (minimum) allowed energy transfer in an intraband transition. The zero- and finite-temperature SPE boundaries are displayed in Fig. 5 by the solid blue and dashed magenta curves, respectively, for four different values of applied electric field. As Figs. 5(a) and 6(a) show, at $\Delta_z = 0$, the SPE region is gapped and the formation of undamped plasmons is possible in the system.

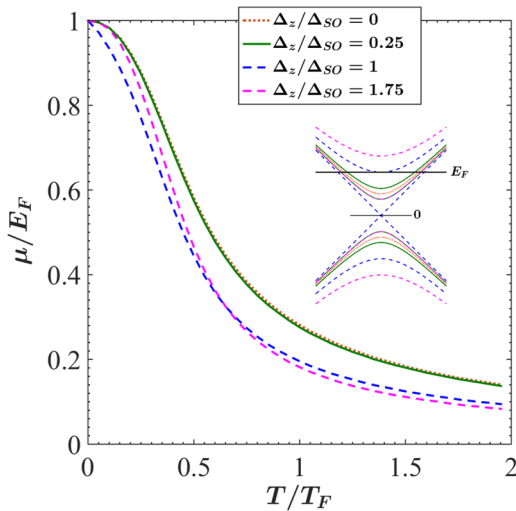


FIG. 4. Scaled chemical potential as a function of dimensionless temperature. As expected, an increase in temperature results in decline of the chemical potential.

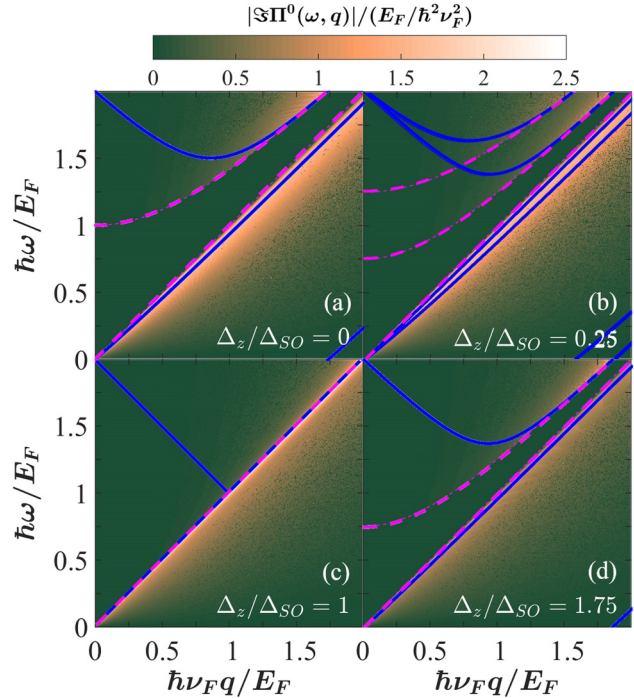


FIG. 5. $\Im\Pi^0(\omega, q)$, scaled by $E_F/(\hbar\nu_F)^2$ for $\Delta_{SO}/E_F = 0.5$ and varying Δ_z/Δ_{SO} : (a) 0, (b) 0.25, (c) 1, and (d) 1.75 at $T/T_F = 0.5$. Solid blue curves show the SPE boundaries at $T = 0$ and dashed magenta curves are those of Eq. (10).

When $\Delta_z/\Delta_{SO} > 0$ [Figs. 5(b)–5(d) and Figs. 6(b)–6(d)], the band structure is spin-split and the polarization function can be interpreted as the summation of two gapped subsystems with bandgaps $2\Delta_{min}$ and $2\Delta_{max}$.⁴⁰ So, similar to $T = 0$ case,^{40,46} the SPE^{Inter} region is divided into two parts such that the lower (upper) boundary corresponds to Δ_{min} (Δ_{max}). With increasing Δ_z , the SPE_{min}^{Inter} boundary moves toward the $\tilde{\omega} = \tilde{q}$ line, while the other one moves away. Furthermore, the intraband boundary, which is located slightly below the $\tilde{\omega} = \tilde{q}$ line, moves toward the $\tilde{\omega} = \tilde{q}$ line very slowly as Δ_z increases. Thus, the SPE gap becomes smaller. This pattern continues until $\Delta_z = \Delta_{SO}$, where the lower boundary of SPE^{Inter} and the SPE^{Intra} boundary meet approximately at the $\tilde{\omega} = \tilde{q}$ line, resulting in closure of the SPE gap as shown in Figs. 5(c) and 6(c). Consequently, at $\Delta_z = \Delta_{SO}$, the possibility of undamped plasmon formation is negligible (except for small q , ω , and T as will be shown later). Figures 5(d) and 6(d) show that as Δ_z grows beyond the Δ_{SO} , the SPE gap opens again: the SPE^{Inter} and SPE^{Intra} boundaries both move away from the $\tilde{\omega} = \tilde{q}$ line. Comparing Figs. 5 and 6 suggests that when the temperature increases from $T = 0.5T_F$ to $T = T_F$, similar to the case of SLGG at finite temperature,⁴⁵ the boundaries are changed only slightly such that the extent of SPE gap decreases by temperature very slowly; this can be explained by the fact that single-particle transitions are more probable at higher temperatures.⁴⁵

Moreover, in panels (a), (b), and (d) of Figs. 5 and 6, the interband boundaries are not discernible before $\tilde{q} \simeq 0.25$, but for

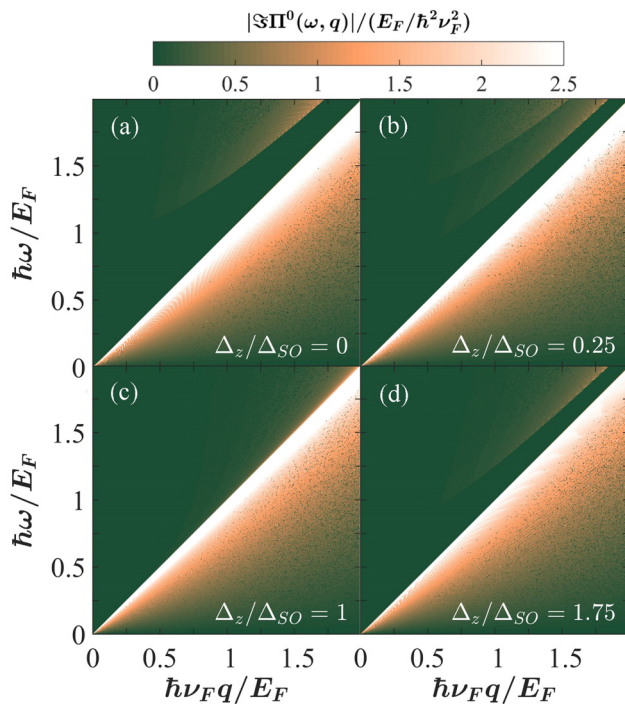


FIG. 6. $\Im\Pi^0(\omega, q)$, scaled by $E_F/(\hbar\nu_F)^2$ for $\Delta_{SO}/E_F = 0.5$ and varying Δ_z/Δ_{SO} : (a) 0, (b) 0.25, (c) 1, and (d) 1.75 at $T/T_F = 1$.

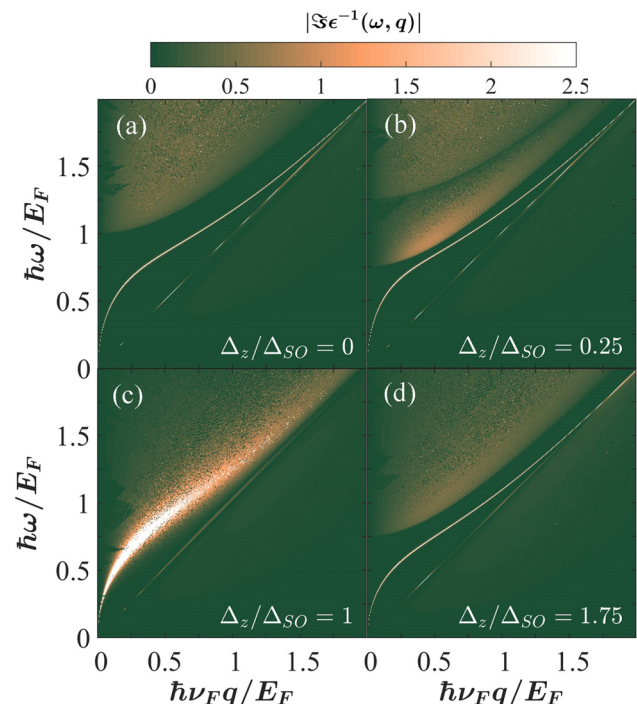


FIG. 7. Loss function of DLS for $\Delta_{SO}/E_F = 0.5$ and varying Δ_z/Δ_{SO} : (a) 0, (b) 0.25, (c) 1, and (d) 1.75 at $T/T_F = 0.5$.

values after that they seem to be consistent with Eq. (10) and the intraband SPE boundary shows consistency with this equation as well. For panel (c), where $\Delta_z/\Delta_{SO} = 1$, Eq. (10) implies that the interband (Δ_{min}) and intraband boundaries lie along $\tilde{\omega} = \tilde{q}$ line, suggesting there is no SPE gap available for long-lived plasmons. This point will be discussed later on.

In order to study the behavior of the finite-temperature plasmonic dispersion in a DLS, we numerically calculate and plot the temperature-dependent DLS loss function, $\Im[\epsilon^{-1}(\omega, q)]$, in the (ω, q) space, for several parameters that affect the band structure. In Fig. 7, the loss function is plotted at $T = 0.5T_F$ for the same parameters as in Fig. 5. Since plasmons are well-defined at small wave vectors, we consider $0 < q < 2E_F/\hbar\nu_F$, corresponding to a range of plasmon energies from 0 to $2E_F$ (0.015eV), which falls in the range of the infrared spectrum. As this figure shows the undamped acoustic and optical plasmon modes exist in the SPE gap for $\Delta_z/\Delta_{SO} = 0, 0.25$, and 1.75 with the acoustic branches having very weak intensity. For $\Delta_z/\Delta_{SO} = 1$, on the other hand, the acoustic and optical branches are broadened for most values of (ω, q) displayed here. Since the SPE gap is almost closed and consequently, the plasmons are damped, there exist narrower peaks only for small q 's, indicating the undamped plasmons.

$\Im[\epsilon^{-1}(\omega, q)]$ for the same parameters as Fig. 7 but at $T = T_F$ is depicted in Fig. 8, where the emergence of new optical modes can be observed. When $\Delta_z/\Delta_{SO} = 0$ [panel (a)], there is only one (undamped) optical branch. However, for $\Delta_z/\Delta_{SO} = 0.25$

[panel (b)] and $\Delta_z/\Delta_{SO} = 1.75$ [panel (d)] where both bandgaps of silicene layers are nonzero, a new undamped optical branch is observed in the vicinity of the SPE_{min}^{inter} 's boundary at higher values of q . Moreover, a new damped mode appears in the weaker damping region of SPE continuum which is not extended from the undamped branch continuously. Such splitting is not obtained for the acoustic branch. At $\Delta_z/\Delta_{SO} = 1$ [panel (c)], we see a similar trend for both branches as observed in Fig. 7(c). However, the branches are generally more broadened because the electron-hole pair excitations are facilitated by increasing temperature.

Plots of the analytical zero-temperature loss function for the same parameters used for Fig. 7 are shown in Fig. 9. The results resemble those in Fig. 7 except for $\Delta_z/\Delta_{SO} = 1$ (VSPM phase), where the undamped optical plasmons are present for a wider range of wave vectors.

To better support the damped and undamped plasmons, we plot the absolute values of the real (a) and imaginary (b) parts of the DLS dynamical dielectric function in the (ω, q) space in Fig. 10 for $\Delta_{SO}/E_F = 0.5$ and $\Delta_z/\Delta_{SO} = 0.25$ at $T = 0.5T_F$. These figures are essentially consistent with those obtained from the loss function but they also demonstrate the presence of a third plasmonic branch,⁶² which is not observable in the plots of the loss function because it is completely located in the Landau damped region.

Figure 11 illustrates the DLS loss function, $\Im(\epsilon^{-1})$, over the (ω, T) plane, at a given $\tilde{q} = 0.1$, for different values of $\Delta_z/\Delta_{SO} = 0, 0.25, 1$, and 1.75 with $\Delta_{SO}/E_F = 0.5$. The upper and lower

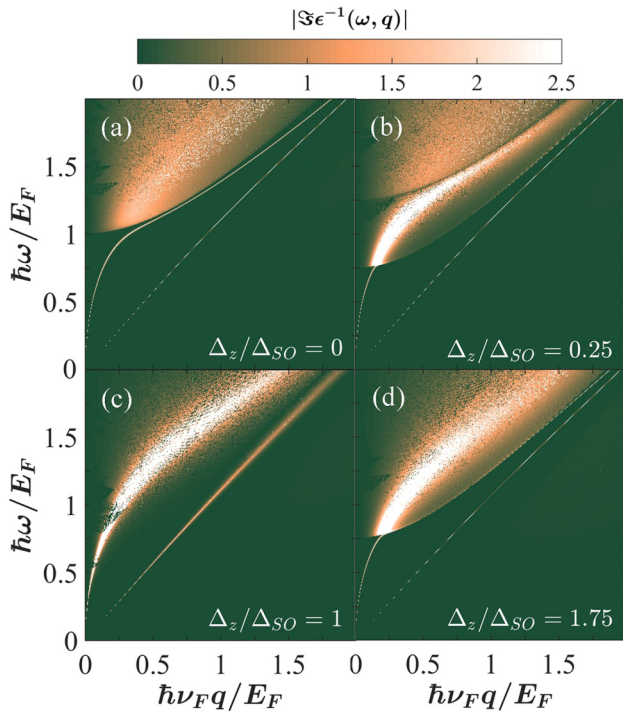


FIG. 8. Loss function of DLS for $\Delta_{SO}/E_F = 0.5$ and varying Δ_z/Δ_{SO} : (a) 0, (b) 0.25, (c) 1, and (d) 1.75 at $T/T_F = 1$.

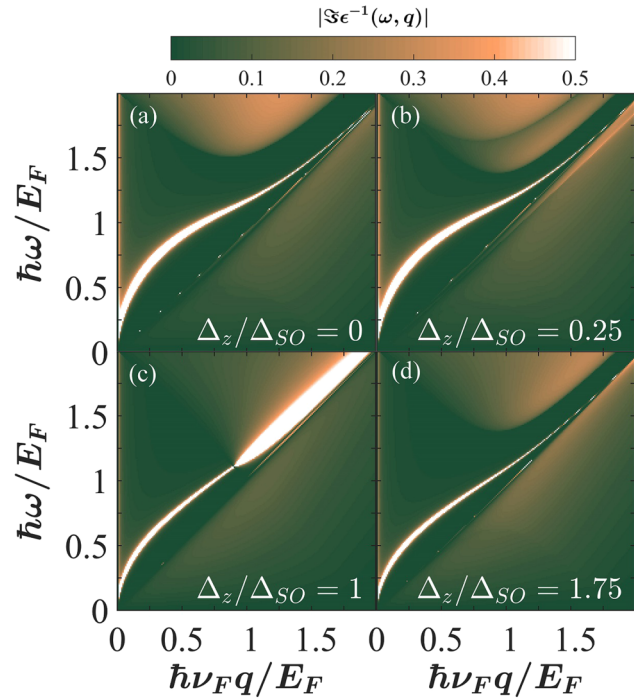


FIG. 9. Loss function of DLS for $\Delta_{SO}/E_F = 0.5$ and varying Δ_z/Δ_{SO} : (a) 0, (b) 0.25, (c) 1, and (d) 1.75 at $T = 0$.

pronounced branches correspond to the optical and acoustic modes, respectively. Figure 12 displays the extent of the SPE boundaries for the same parameters. As can be observed from these figures, the optical branches are positioned in the SPE gap and, therefore, remain undamped for all presented values of T , except for the VSPM phase. Furthermore, the frequency of the optical branch decreases with an increase in temperature and reaches a minimum value around $T = 0.4T_F$ but after that it bounces off at higher temperatures. The behavior of optical plasmons for this studied DLS is similar to the plasmon dispersion of SLGG, where the plasmon frequencies follow first a decreasing and then an increasing trend with a minimum at $T \sim 0.5T_F$ for all bandgap values⁴⁵ and similar to the double-layer graphene at small wave vectors.⁵⁶ Recently, it has been shown that the temperature-dependent plasmons of SLS, SLG, and single-layer n-doped and p-doped molybdenum disulfide can also exhibit such a behavior.⁴¹

In Fig. 11(c), for $\Delta_z/\Delta_{SO} = 1$, the optical branch follows a similar temperature trend as the other phases, but Fig. 12(c) shows that there is almost no gap left for the undamped plasmons to reside. However, for $T = 0$ and low temperatures, SPE^{Inter} boundary sits higher than the approximate interband SPE boundary. Thus, as can be seen, for $T/T_F < 0.1$, the optical branch has a well-defined delta function-like peak, which is a characteristic of undamped plasmons. Beyond this temperature, however, the peak is extremely broadened which indicates damping of plasmons at higher temperatures. Moreover, Fig. 11 demonstrates the fact that

the spectral weight of acoustic mode is insignificant compared to that of optical mode; this is an obstacle in experimentally observing the acoustic mode. Applying a more distinguishing color limit to all panels of Fig. 11 reveals that the acoustic branches located in close proximity of SPE^{Intra} boundary grow negligibly with temperature, which may not be of experimental significance. This figure

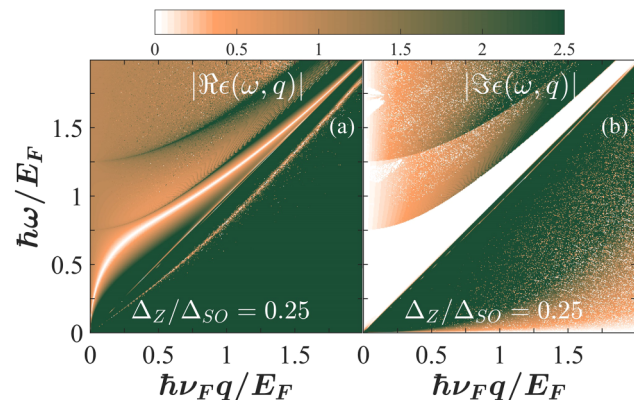


FIG. 10. Dielectric function of DLS for $\Delta_{SO}/E_F = 0.5$ and $\Delta_z/\Delta_{SO} = 0.25$ at $T = 0.5T_F$: (a) real part and (b) imaginary part.

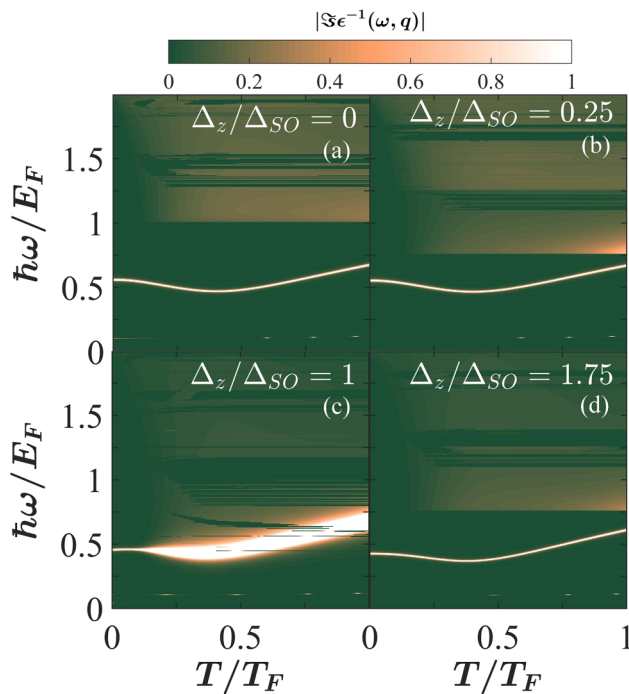


FIG. 11. Loss function of DLS as a function of (ω, T) for $\Delta_{SO}/E_F = 0.5$ and two different values of Δ_z/Δ_{SO} : (a) 0.25 and (b) 1 at $\tilde{q} = 0.1$.

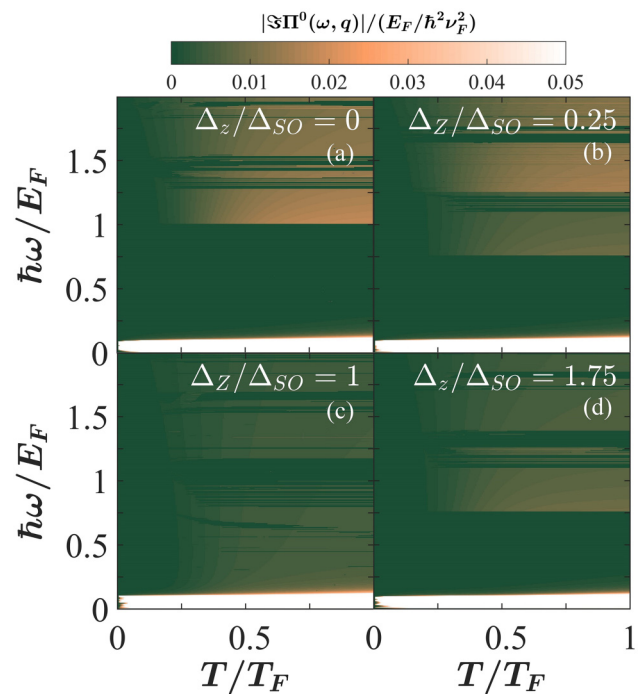


FIG. 12. $\Im\Pi^0$ as a function of (ω, T) , scaled by $E_F/(\hbar v_F)^2$ for $\Delta_{SO}/E_F = 0.5$ and two different values of Δ_z/Δ_{SO} : (a) 0.25 and (b) 1 at $\tilde{q} = 0.1$.

also displays that as temperature rises, the interband boundary changes a bit and the intraband boundary moves slightly to higher frequencies.

To investigate the effect of spatial separation between two layers on the DLS plasma oscillation modes, we plot $\Im\epsilon^{-1}$ in the (ω, d) plane at $\tilde{q} = 0.1$ for $\Delta_{SO}/E_F = 0.5$ and $\Delta_z/\Delta_{SO} = 0.25$ in Fig. 13 at two different temperatures, $T = 0.5T_F$ and T_F . The inter-layer separation varies from 50 Å up to 150 Å in this figure. As demonstrated, for all the presented separation values at both temperatures, the undamped acoustic and optical modes exist (with a very weak acoustic mode spectral weight). Figure 13 suggests that the finite-temperature optical modes are not affected by changing the spatial separation between the layers, similar to the zero-temperature case. On the other hand, applying a more distinguishing colormap displays that the frequency of acoustic plasmons increases slightly with d for both temperatures such that $T = T_F$ dispersion has a slightly higher slope. This growth is also observed at $T = 0$, which is evident from the d -dependence of Eq. (9). Our results here may not be easily observed in experiment, though.

In order to study the effect of an external electric field on the finite-temperature DLS plasmons, the loss function is plotted in Fig. 14 for $\Delta_{SO}/E_F = 0.5$ with $T = 0.5T_F$ and T_F at $\tilde{q} = 0.1$. At both temperatures, the optical plasmon frequency decreases as Δ_z increases quite similar to the trend for $T = 0$ (see Fig. 3). Moreover, the optical plasmon branch enters the SPE region for a certain interval of Δ_z/Δ_{SO} around $\Delta_z/\Delta_{SO} = 1$ and this interval is extended as the temperature increases from $T = 0.5T_F$ up to

$T = T_F$. It can also be seen that the damped part of the optical plasmon branch is not extended continuously from the undamped part, and it really seems more like a separate mode; for the acoustic branch, however, such discontinuity cannot be observed as it enters and exits the SPE region.

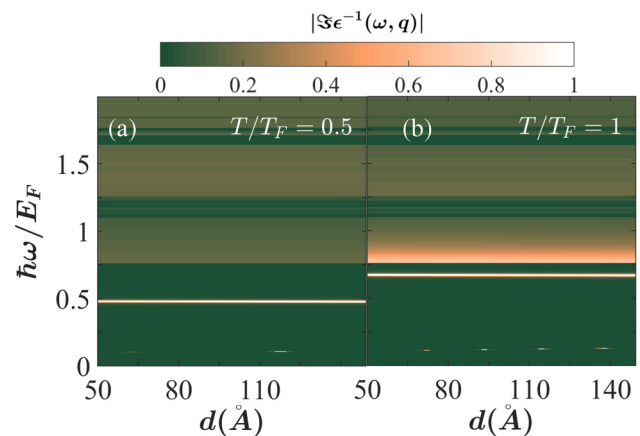


FIG. 13. Loss function of DLS as a function of (ω, d) at $\tilde{q} = 0.1$, for $\Delta_{SO}/E_F = 0.5$ and $\Delta_z/\Delta_{SO} = 0.25$ at two different values of T/T_F : (a) 0.5 and (b) 1.

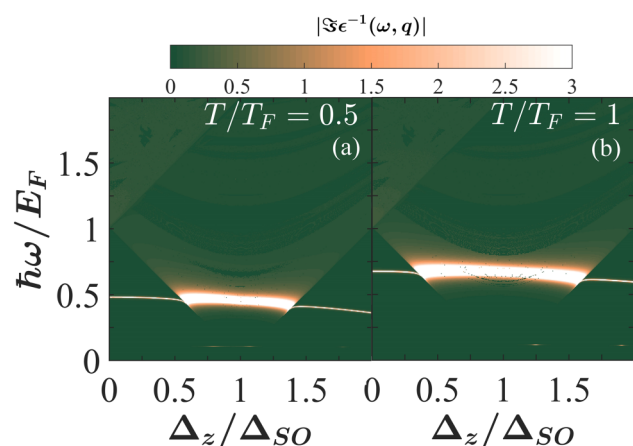


FIG. 14. Loss function of DLS as a function of (ω, Δ_z) at $\tilde{q} = 0.1$ for $\Delta_{SO}/E_F = 0.5$ at two different values of T/T_F : (a) 0.5 and (b) 1.

IV. CONCLUSION

To summarize, we have studied the finite-temperature plasmons of an n-doped double-layer 2D system consisting of silicene sheets with $\Delta_{SO} = 3.9$ meV and $\Delta_{SO}/E_F = 0.5$. We have considered all three phases of silicene (TI, VSPM, and BI) by applying an external electric field to the system. For comparison, the zero-temperature results have been presented. By calculating the poles of the loss function, both the optical and acoustic plasmon branches have been obtained. To illustrate the finite-temperature SPE regions, we have also plotted the imaginary part of the polarization function. Our calculations for a DLS with $d = 100$ Å have shown that as the temperature is raised from 0 up to T_F , the optical plasmon frequency first decreases and then increases smoothly for the different values of $\Delta_z/\Delta_{SO} = 0$ (TI), 0.25 (TI), 1 (VSPM), and 1.75 (BI). However, the acoustic modes change negligibly with temperature. Moreover, for a DLS with $\Delta_z/\Delta_{SO} = 0.25$ at finite temperature, similar to the zero-temperature analytical results at long wavelengths, the optical plasmon dispersion is unaffected by the change in the layer separation, at both $T = 0.5T_F$ and $T = T_F$, while the acoustic plasmon dispersion exhibits a small growth. The effect of external electric field has also been studied for $T = 0.5T_F$ and T_F at a given q , and a decreasing trend has been observed for the optical plasmon dispersion as Δ_z/Δ_{SO} varies from 0 to 2 and a Landau damping behavior is obtained around $\Delta_z/\Delta_{SO} = 1$. The corresponding zero-temperature results have displayed a discontinuity at the VSPM phase for both optical and acoustic plasmons.

REFERENCES

- ¹G. G. Guzmán-Verri and L. C. Lew Yan Voon, *Phys. Rev. B* **76**, 075131 (2007).
- ²S. Cahangirov, M. Topsakal, E. Aktürk, H. Şahin, and S. Ciraci, *Phys. Rev. Lett.* **102**, 236804 (2009).
- ³H. Enriquez, S. Vizzini, A. Kara, B. Lalmi, and H. Oughaddou, *J. Phys. Condens. Matter* **24**, 314211 (2012).
- ⁴D. Kaltsas and L. Tsetseris, *Phys. Chem. Chem. Phys.* **15**, 9710 (2013).

- ⁵L. C. Lew Yan Voon, J. Zhu, and U. Schwingenschlögl, *Appl. Phys. Rev.* **3**, 040802 (2016).
- ⁶S. Huang, W. Kang, and L. Yang, *Appl. Phys. Lett.* **102**, 133106 (2013).
- ⁷M. Barati, T. Vazifeshenas, T. Salavati-fard, and M. Farmanbar, *J. Phys. Condens. Matter* **30**, 155307 (2018).
- ⁸A. Kara, C. Léandri, M. E. Dávila, P. De Padova, B. Ealet, H. Oughaddou, B. Aufray, and G. Le Lay, *J. Supercond. Nov. Magn.* **22**, 259 (2009).
- ⁹H. Nakano and T. Ikuno, *Appl. Phys. Rev.* **3**, 040803 (2016).
- ¹⁰Y. Sugiyama, H. Okamoto, T. Mitsuoka, T. Morikawa, K. Nakanishi, T. Ohta, and H. Nakano, *J. Am. Chem. Soc.* **132**, 5946 (2010).
- ¹¹C. L. Lin, R. Arafune, K. Kawahara, N. Tsukahara, E. Minamitani, Y. Kim, N. Takagi, and M. Kawai, *Appl. Phys. Express* **5**, 5 (2012).
- ¹²B. Feng, Z. Ding, S. Meng, Y. Yao, X. He, P. Cheng, L. Chen, and K. Wu, *Nano Lett.* **12**, 3507 (2012).
- ¹³D. Chiappe, C. Grazianetti, G. Tallarida, M. Fanciulli, and A. Molle, *Adv. Mater.* **24**, 5088 (2012).
- ¹⁴H. Jamgotchian, Y. Colignon, N. Hamzaoui, B. Ealet, J. Y. Hoarau, B. Aufray, and J. P. Bibérian, *J. Phys. Condens. Matter* **24**, 172001 (2012).
- ¹⁵A. Fleurence, R. Friedlein, T. Ozaki, H. Kawai, Y. Wang, and Y. Yamada-Takamura, *Phys. Rev. Lett.* **108**, 245501 (2012).
- ¹⁶L. Meng, Y. Wang, L. Zhang, S. Du, R. Wu, L. Li, Y. Zhang, G. Li, H. Zhou, W. A. Hofer, and H.-J. Gao, *Nano Lett.* **13**, 685 (2013).
- ¹⁷B. Lalmi, H. Oughaddou, H. Enriquez, A. Kara, S. Vizzini, B. Ealet, and B. Aufray, *Appl. Phys. Lett.* **97**, 223109 (2010).
- ¹⁸Z. Ni, Q. Liu, K. Tang, J. Zheng, J. Zhou, R. Qin, Z. Gao, D. Yu, and J. Lu, *Nano Lett.* **12**, 113 (2012).
- ¹⁹N. D. Drummond, V. Zolyomi, and V. I. Fal'ko, *Phys. Rev. B* **85**, 075423 (2012).
- ²⁰W.-F. Tsai, C.-Y. Huang, T.-R. Chang, H. Lin, H.-T. Jeng, and A. Bansil, *Nat. Commun.* **4**, 1500 (2013).
- ²¹X. Zhai and G. Jin, *J. Phys. Condens. Matter* **28**, 355002 (2016).
- ²²X.-Q. Wu and H. Meng, *J. Appl. Phys.* **117**, 203903 (2015).
- ²³B. Soodchomshom, *J. Appl. Phys.* **115**, 023706 (2014).
- ²⁴L. Tao, E. Cinquanta, D. Chiappe, C. Grazianetti, M. Fanciulli, M. Dubey, A. Molle, and D. Akinwande, *Nat. Nanotechnol.* **10**, 1 (2015).
- ²⁵B. N. Narozhny and A. Levchenko, *Rev. Mod. Phys.* **88**, 025003 (2016).
- ²⁶L. Zheng and A. H. MacDonald, *J. Phys. Condens. Matter* **24**, 335602 (2012).
- ²⁷L. Zheng and A. H. MacDonald, *Phys. Rev. B* **48**, 8203 (1993).
- ²⁸S. Saberi-Pouya, T. Vazifeshenas, M. Farmanbar, and T. Salavati-fard, *J. Phys. Condens. Matter* **28**, 285301 (2016).
- ²⁹T. Vazifeshenas and T. Salavati-fard, *Physica B* **462**, 112 (2015).
- ³⁰K. Güven and B. Tanatar, *Phys. Rev. B* **56**, 7535 (1997).
- ³¹R. Gorbachev, A. Geim, M. Katsnelson, K. Novoselov, T. Tudorovskiy, I. Grigorieva, A. MacDonald, S. Morozov, K. Watanabe, T. Taniguchi, and L. Ponomarenko, *Nat. Phys.* **8**, 896 (2012).
- ³²E. H. Hwang and S. Das Sarma, *Phys. Rev. B* **80**, 205405 (2009).
- ³³N. M. R. Peres, J. M. B. L. dos Santos, and A. H. C. Neto, *Europhys. Lett.* **95**, 18001 (2011).
- ³⁴Y. W. Suen, L. W. Engel, M. B. Santos, M. Shayegan, and D. C. Tsui, *Phys. Rev. Lett.* **68**, 1379 (1992).
- ³⁵S. Kim, I. Jo, J. Nah, Z. Yao, S. K. Banerjee, and E. Tutuc, *Phys. Rev. B* **83**, 161401 (2011).
- ³⁶K. Flensberg and B. Y.-K. Hu, *Phys. Rev. B* **52**, 14796 (1995).
- ³⁷S. Das Sarma and A. Madhukar, *Phys. Rev. B* **23**, 805 (1981).
- ³⁸T. Vazifeshenas, T. Amlaki, M. Farmanbar, and F. Parhizgar, *Phys. Lett. A* **374**, 4899 (2010).
- ³⁹J.-Y. Wu, C.-Y. Lin, G. Gumbs, and M.-F. Lin, *RSC Adv.* **5**, 51912 (2015).
- ⁴⁰C. J. Tabert and E. J. Nicol, *Phys. Rev. B* **89**, 195410 (2014).
- ⁴¹A. Iurov, G. Gumbs, and D. Huang, *J. Phys. Condens. Matter* **29**, 135602 (2017).
- ⁴²A. Iurov, G. Gumbs, D. Huang, and G. Balakrishnan, *Phys. Rev. B* **96**, 245403 (2017).
- ⁴³H. R. Chang, J. Zhou, H. Zhang, and Y. Yao, *Phys. Rev. B* **89**, 201411 (2014).

- ⁴⁴P. K. Pyatkovskiy, *J. Phys. Condens. Matter* **21**, 025506 (2009).
- ⁴⁵D. K. Patel, S. S. Ashraf, and A. C. Sharma, *Phys. Status Solidi B* **252**, 1817 (2015).
- ⁴⁶B. Van Duppen, P. Vasilopoulos, and F. M. Peeters, *Phys. Rev. B* **90**, 035142 (2014).
- ⁴⁷Z. Qiao, S. A. Yang, W. Feng, W.-K. Tse, J. Ding, Y. Yao, J. Wang, and Q. Niu, *Phys. Rev. B* **82**, 161414 (2010).
- ⁴⁸H. Haugen, D. Huertas-Hernando, and A. Brataas, *Phys. Rev. B* **77**, 115406 (2008).
- ⁴⁹T. Yokoyama, *New J. Phys.* **16**, 085005 (2014).
- ⁵⁰M. Mirzaei, T. Vazifeshenas, T. Salavati-fard, M. Farmanbar, and B. Tanatar, *Phys. Rev. B* **98**, 045429 (2018).
- ⁵¹T. Stauber and G. Gómez-Santos, *Phys. Rev. B* **85**, 075410 (2012).
- ⁵²R. E. V. Profumo, R. Asgari, M. Polini, and A. H. MacDonald, *Phys. Rev. B* **85**, 085443 (2012).
- ⁵³G. Gumbs, A. Iurov, M. F. Lin, and P. Fekete, *Sci. Rep.* **6**, 21063 (2016).
- ⁵⁴E. H. Hwang and S. Das Sarma, *Phys. Rev. B* **75**, 205418 (2007).
- ⁵⁵S. Das Sarma and E. H. Hwang, *Phys. Rev. Lett.* **102**, 206412 (2009).
- ⁵⁶D. Van Tuan and N. Q. Khanh, *Physica E* **54**, 267 (2013).
- ⁵⁷S. M. Badalyan and F. M. Peeters, *Phys. Rev. B* **85**, 195444 (2012).
- ⁵⁸C. L. Kane and E. J. Mele, *Phys. Rev. Lett.* **95**, 1 (2005).
- ⁵⁹M. Ezawa, *Phys. Rev. B* **87**, 155415 (2013).
- ⁶⁰C. C. Liu, H. Jiang, and Y. Yao, *Phys. Rev. B* **84**, 195430 (2011).
- ⁶¹M. Ezawa, *New J. Phys.* **14**, 033003 (2012).
- ⁶²C. Vacacela Gomez, M. Pizarra, M. Gravina, P. Riccardi, and A. Sindona, *Phys. Rev. B* **95**, 085419 (2017).
- ⁶³A. Sindona, M. Pizarra, C. Vacacela Gomez, P. Riccardi, G. Falcone, and S. Bellucci, *Phys. Rev. B* **96**, 201408 (2017).
- ⁶⁴J. P. Reed, B. Uchoa, Y. I. Joe, Y. Gan, D. Casa, E. Fradkin, and P. Abbamonte, *Science* **330**, 805 (2010).
- ⁶⁵Y. Gan, G. A. de la Peña, A. Kogar, B. Uchoa, D. Casa, T. Gog, E. Fradkin, and P. Abbamonte, *Phys. Rev. B* **93**, 195150 (2016).
- ⁶⁶C. Hwang, D. A. Siegel, S.-K. Mo, W. Regan, A. Ismach, Y. Zhang, A. Zettl, and A. Lanzara, *Sci. Rep.* **2**, 590 (2012).